RSC Advances

ROYAL SOCIETY OF CHEMISTRY

www.rsc.org/advances

Nanostructured nickel sulfides: Phase evolution, characterization and electrocatalytic properties for the hydrogen evolution reaction

Yuan Pan, Yinjuan Chen, Xiao Li, Yunqi Liu, Chenguang Liu**

State Key Laboratory of Heavy Oil Processing, Key Laboratory of Catalysis, China National Petroleum Corporation (CNPC), China University of Petroleum, 66 West Changjiang Road, Qingdao, Shandong 266580, P. R. China

* Corresponding author. E-mail address: liuyq@upc.edu.cn; cgliu1962@sina.com

Tel.: +86-532-86981861; +86-532-86981716.

Abstract

Nanostructured nickel sulfide with different phases were synthesized via a thermal decomposition approach using nickel acetylacetonate as the nickel source, 1-dodecanethiol as the sulfur source and oleylamine as the high boiling solvent. The phase evolution of nickel sulfide nanocrystals (NCs) can be easily achieved by changing the molar ratio of Ni:S precursor and the species of solvent. X-ray diffraction (XRD), transmission electron microscopy (TEM), scanning electron microscope (SEM), energy dispersive spectrum (EDS) mapping, X-ray photoelectron spectroscopy (XPS) and N_2 adsorption-desorption were used to characterize the as-synthesized nickel sulfide NCs. The electrocatalytic activity and stability of the as-synthesized nickel sulfide NCs for the hydrogen evolution reaction (HER) were investigated. Due to the different crystalline phase structure of the as-synthesized nickel sulfide NCs, the β NiS NCs exhibit better electrocatalytic activity with a low onset overpotential (186 mV), a small Tafel slope (51.2 $mV \cdot dec^{-1}$), a high exchange current density (2.4×10^{-6} $A \cdot cm^{-2}$), a large electrochemical double-layer capacitances (2.7 $mF \cdot cm^{-2}$) and good stability than the Ni_7S_6 and α NiS + β NiS NCs for HER. This study provides a good strategy for designing more efficient nickel sulfide catalysts for the HER.

Keywords: Nickel sulfide; phase evolution; electrocatalyst; hydrogen evolution reaction

1 Introduction

Nowadays, electrolysis of water plays an extremely important role to produce hydrogen in the fast-developing field of new energy due to more stringent environmental regulations[1]. There is no doubt that Pt-based noble metal is the most efficient catalyst for the hydrogen evolution reaction (HER). However, large scale application was limited due to the high price and low abundance of Pt-based noble metal[2]. Therefore, the development of non-noble metal catalysts with low cost and high abundance are needed. In recent years, all kinds of non-noble metal materials have been used as HER catalysts, such as metal sulfides[3], metal phosphides[4] and metal carbides[5]. It has been reported that nanostructured metal sulfides are good alternatives due to their unique physicochemical properties[6]. As a representative of metal sulfides, nickel sulfide-based nanomaterials exhibit excellent catalytic properties, which indicates that the research of metal sulfides will become very attractive in the future[7]. As we all know, nickel sulfides contain different atomic configurations and crystalline structures, such as Ni_9S_8, Ni_7S_6, Ni_3S_2, NiS, NiS_2, Ni_3S_4 and so on. In order to enhance the catalytic performance of HER catalysts, a considerable attention have been paid to optimize their structure and morphology. In addition, it has been reported that the crystalline phase structure play an important role in catalytic properties. For example, Su et al. reported that the phase-dependent catalytic properties of manganese oxide catalysts for the oxygen reduction reaction (ORR) and oxygen evolution reaction (OER)[8]. Wang et al. reported that cobalt sulfides with different phases exhibit different performance in lithium ion batteries[9]. Schaak group reported that

nanostructured cobalt phosphide with different phases exhibit different electrocatalytic activities for the HER[10]. Our previously work also reported that the phase-dependent catalytic activity of nickel phosphide nanocrystals (NCs) for the HER[11]. Therefore, we think that the research of phase-dependent catalytic properties of nickel sulfide NCs for HER is meaningful and the relevant reports are rare.

In this study, we have successfully synthesized nickel sulfide NCs with different phases via a thermal decomposition approach using nickel acetylacetonate as the nickel source, 1-dodecanethiol as the sulfur source and oleylamine as the solvent. The phase evolution process was achieved by changing the precursor ratio and the species of solvent. X-ray diffraction (XRD), transmission electron microscopy (TEM), scanning electron microscope (SEM), energy dispersive spectrum (EDS) mapping, X-ray photoelectron spectroscopy (XPS), and N_2 adsorption-desorption were used to characterize the as-synthesized nickel sulfide NCs. In addition, the phase-dependent of the nickel sulfide NCs on the electrocatalytic properties for HER were investigated systematically. The different phases result in different catalytic activities for HER, as shown by experiments. This work indicates that the phase-dependent catalytic activity is important for designing new catalysts for HER.

2 **Experimental**

2.1 Phase evolution of nickel sulfide NCs

In a typical synthesis, under a flow of argon, 0.385 g nickel acetylacetonate ($Ni(acac)_2$, Aldrich, 95%), 2 mL 1-dodecanethiol (Aldrich, 90%) and 10 mL oleylamine (OAm, Aldrich, 90%) were put into a 100 mL four-necked flask. The

mixture was stirred magnetically and then heated to 280 ^{o}C for 5 h. The as-obtained mixture was separated by centrifugation using the mixture of hexane and ethanol. Finally, the product was obtained by drying in vacuum at 60 ^{o}C for 24 h. The crystalline phase evolution of nickel sulfide NCs can be achieved by changing the Ni:S precursor ratio and the species of solvent, while the other conditions were not changed.

2.2 Characterization

The crystalline phase structure was confirmed by XRD, which was collected on a panalytical X'pert PROX-ray diffractometer with Cu Kα monochromatized radiation (λ= 1.54 Å). The morphology and composition were characterized by TEM, SEM and EDS mapping, which were collected on a JEM-2100 UHR microscope and JSM-7500F (JEOL, Japan) instrument. The textural property was characterized by N_2 adsorption-desorption experiments, which were carried out on a ChemBET 3000 (Quantachrome, USA) instrument. Nitrogen sorption isotherms were measured at -196 °C by the volumetric method. Prior to the measurement, the as-synthesized samples were evacuated at 300 °C for 6 h on a vacuum line. The surface area of the samples were measured by the Brunauer-Emmet-Teller (BET) method. The pore size distributions of the samples were derived from the desorption branch of the isotherms according to the Barett-Joyner-Halenda (BJH) model. The chemical valence state was confirmed by XPS, which was performed on a VG ESCALABMK II spectrometer (Al Ka).

2.3 Electrochemical measurements

The HER electrocatalytic activity of the as-synthesized nickel sulfide NCs with different phases was performed in nitrogen-purged 0.5 M H_2SO_4 at room temperature using a standard three-electrode setup (Reference 600 Gamry Instruments, USA). The working electrode was the as-obtained sample, which was modified by the glassy carbon electrode (GCE, 4 mm in diameter). The working electrode was prepared as follows: 5 mg of catalyst and 20 μL Nafion solution (5 wt %) were dispersed in 1 mL ethanol by sonicating for 30 min to form a homogeneous ink. Then 5 μL of the dispersion solution was loaded onto a GCE surface. The catalyst-modified GCE was dried at room temperature to yield a catalyst loading of 199 $\mu g \cdot cm^{-2}$. The reference electrode was Ag/AgCl electrode and the counter electrode was Pt electrode. In all the measurements, the Ag/AgCl reference electrode was checked using the reversible hydrogen electrode (RHE). Namely, in 0.5 M H_2SO_4 solution, E (V vs. RHE) = E (V vs. Ag/AgCl) + 0.222 V + 0.059 pH = E (V vs. Ag/AgCl) + 0.222 V. The linear sweep voltammetry (LSV) was performed in 0.5 M H_2SO_4 solution from -0.6 to 0 V vs RHE with scan rate of 5 $mV \cdot s^{-1}$. Because the as-measured currents cannot directly reflect the intrinsic behavior of the as-synthesized electrocatalysts because of the effect of ohmic resistance, an (iR) correction was applied to the measured polarization curves. The data have been corrected according to the equation: $E_a = E_b - iR_s$, where E_a is the overpotential after iR correction, E_b is the overpotential before iR correction, i is the corresponding current and R_s is the resistance of the system obtained from electrochemical impedance spectroscopy plots. The cycling stability test was conducted by cyclic voltammetry (CV) scanning 1000 cycles from -0.4 ~ 0.2 V (vs.

Ag/AgCl) in 0.5 M H_2SO_4 with a scan rate of 50 $mV \cdot s^{-1}$. The double layer capacitance (C_{dl}) was carried out with a simple cyclic voltammetry (CV) scanning in 0.5 M H_2SO_4 from 0.1 to 0.2 V vs RHE with different scan rate from 20 to 180 $mV \cdot s^{-1}$. The electrochemical impedance spectroscopy (EIS) experiments were performed in 0.5 M H_2SO_4 with frequencies ranging from 100 kHz to 0.1 Hz with an AC voltage of 5 mV at different potential. The as-obtained EIS data were fitted using Zsimpwin software.

3 Results and discussion

3.1 Phase evolution and characterization of nickel sulfide NCs

In our experiments, a one-pot thermal decomposition approach was used to synthesize the nickel sulfide NCs. We carried out several groups of the single-factor experiment to control the crystalline phase of nickel sulfide NCs. Table 1 shows the synthetic conditions and the corresponding product for each group. It can be found that the phase evolution of nickel sulfide NCs can be easily achieved by changing the Ni:S precursor ratio and the solvent species. With the decrease of Ni:S precursor ratio from 0.36 to 0.08, the crystal phase was changed from Ni_7S_6 to β NiS. In our reaction system, 1-dodecanethiol acted as the sulfide source as well as a strong ligand, which can adsorb on the surface of nickel precursor. When the reaction temperature was 280°C, the S-C bonds broke and sulfide atoms formed, which can diffuse into the nickel precursor. The combination of nickel and sulfide lead to the formation of nickel sulfide NCs. In addition, the decrease of Ni:S precursor ratio is favorable to the diffusion of sulfide atoms, which lead to the formation of sulfide rich NiS NCs.

Furthermore, we found that the solvent is another factor to influence the crystal phase. For instance, Ni_7S_6 NCs were obtained by using OAm as solvent. However, both α NiS and β NiS NCs were obtained by using ODE as solvent. This result indicates that the crystal phase of nickel sulfide also can be affected by the molecular structure of the coordinating solvent. The reason can be attributed to the different capping ability of two solvent[12]. In our reaction system, OAm is coordinating solvent, ODE is noncoordinating solvent. The capping ability of ODE is weaker than OAm, thus, ODE can accelerate the diffusion of sulfur derived from 1-dodecanethiol into the nickel precursor, which lead to the formation of NiS NCs.

The crystalline phase structure and purity of the as-synthesized nickel sulfide NCs were characterized by XRD. Fig. 1 shows the XRD patterns of the as-synthesized nickel sulfide NCs at different Ni:S precursor ratio and solvent. When the Ni:S precursor ratio was 0.36, all the diffraction peaks matched well with Ni_7S_6 (PDF#00-014-0364). When the Ni:S precursor ratio was decreased to 0.18, the crystalline phase was not changed. Further decreasing the Ni:S precursor ratio to 0.08, all the diffraction peaks matched well with the rhombohedral structure of β NiS (PDF#01-086-2280), the diffraction peaks at 18.5°, 30.3°, 32.2°, 35.8°, 37.5°, 40.6°, 48.9°, 50.2°, 52.7°, 56.3°, 57.6°, 59.7°, 66.3°, 67.5°, 70.6° and 72.6° can be attributed to (110), (101), (300), (021), (220), (211), (131), (410), (401), (321), (330), (012), (241), (600), (520) and (312) crystal faces. No additional peaks of other phases were found, indicating the high purity of the as-synthesized β NiS. In addition, when OAm was replaced by ODE, different crystalline phase was observed. All the diffraction

peaks matched well with the rhombohedral structure of β NiS (major) and the hexagonal structure of α NiS (minor), the diffraction peaks at 34.6°, 45.7° and 53.4° are attributed to (101), (102) and (110) crystal faces of α NiS (PDF#01-077-1624). Thus, it can be concluded that the crystalline structure of nickel sulfide NCs can be controlled by changing the Ni:S precursor ratio and the species of solvent.

TEM, SEM and the corresponding EDS element mapping were used to characterize the morphology and composition of the as-synthesized nickel sulfide NCs. Fig. 2 shows the TEM images of nickel sulfide NCs synthesized at different conditions. The rod-shaped Ni_7S_6 NCs with an average length of 50 nm were obtained at the Ni:S precursor ratio of 0.36, but the nanorods were not very uniform (Fig. 2A). Decreasing the Ni:S precursor ratio to 0.18, the rod-shaped morphologies of Ni_7S_6 NCs were not changed (Fig. 2B). The corresponding HRTEM image (Fig. 2C) reveals that the fringe spacing is about 2.88 Å, corresponding to the (121) lattice planes of Ni_7S_6 NCs. However, when the Ni:S precursor ratio was decreased to 0.08, highly branched rod-shaped β NiS NCs with an average length of 100 nm were obtained (Fig. 2D). The corresponding HRTEM image (Fig. 2E) reveals that the fringe spacing is about 1.87 Å, corresponding to the (131) lattice planes of β NiS NCs. These results indicate that the morphologies of nickel sulfide NCs were not changed with the decrease of Ni:S precursor ratio. However, by using ODE as a solvent, α NiS + β NiS nanoparticles with the size of about 50 nm were obtained (Fig. 2F), but the obtained particles are not uniform. These results indicate the morphologies of nickel sulfide NCs could be controlled by changing the solvent. In addition, the highly branched rod-shaped

morphologies of β NiS NCs also were confirmed by SEM (Fig. 2G and H). The selected area elemental mapping reveals that the uniform distribution of Ni (Fig. 2I) and S (Fig. 2J) elements in β NiS NCs. Furthermore, EDS (Fig. 2K) also confirms the presence of Ni and S elements. The measured atomic Ni:S ratio is 14.42:14.87, which is very close to the stoichiometric ratio of 1:1 in NiS.

The textural properties of the as-synthesized nickel sulfide NCs with different phases were studied by N_2 adsorption-desorption isotherms (Fig. 3A). β NiS NCs showed a type-IV isotherm with H1-type hysteresis loop at relative pressures (P/P_0) ranging from 0.4 to 0.9, which is typical for a mesoporous materials[13]. Ni_7S_6 and α NiS + β NiS NCs exhibit a type-IV isotherm with a sharp capillary condensation step in the relative pressure (P/P_0) range from 0.4 to 1.0, and the hysteresis loop exhibits a H3-type, which indicates that there are large macropores and mesopores in the materials[14, 15]. In addition, the adsorption of β NiS NCs is higher than that of Ni_7S_6 and α NiS + β NiS NCs, which indicates that the β NiS NCs have higher specific surface area. The BJH pore-size distribution (Fig. 3B) of the Ni_7S_6, α NiS + β NiS and β NiS NCs showed the average pore size are 12.3, 11.5 and 5.3 nm, respectively, further confirming that the as-synthesized nickel sulfides have a mesoporous structure[16]. The BET specific surface area of β NiS NCs was calculated to be 30.4 $m^2 \cdot g^{-1}$, which is higher than that of α NiS + β NiS NCs (20.3 $m^2 \cdot g^{-1}$) and Ni_7S_6 NCs (17.6 $m^2 \cdot g^{-1}$). The higher surface area of β NiS NCs indicates that it exposed more active sites and exhibited higher catalytic performance for HER[17].

The chemical composition and state of the as-synthesized nickel sulfide NCs were

characterized by XPS. Fig. 4A-F show the XPS spectra in the Ni 2p and S 2p regions of the as-synthesized β NiS, α NiS + β NiS and Ni_7S_6 NCs, respectively. For the Ni 2p region (Fig. 4A), the peaks observed at binding energy 854.7 and 872.2 eV are assigned to the Ni $2p_{3/2}$ and Ni $2p_{1/2}$ energy levels of β NiS[18]. The peaks at 857.9 and 876.4 eV can be attributed to oxidized Ni species formed on the surface of β NiS NCs. In addition, two peaks were observed at 862 and 881.5 eV, which can be assigned to the satellite peaks of Ni 2p in β NiS. For the S 2p region (Fig. 4B), two peaks observed at 161.1 and 162.3 eV agree well with S $2p_{3/2}$ and S $2p_{1/2}$ of β NiS NCs[19]. The broad peak observed at 168.2 eV can be assigned to oxidized S species formed on the surface of β NiS because the sample was exposed to air. Furthermore, we also found that the α NiS + β NiS (Fig. 4C and D) and Ni_7S_6 NCs (Fig. 4E and F) have similar Ni 2p and S 2p energy levels to those of β NiS NCs except for the energy levels have small shift. For example, the Ni $2p_{3/2}$ energy levels of α NiS + β NiS and Ni_7S_6 NCs were located at 853.1 and 852.8 eV, respectively, which indicates that the positive charge value (δ) of Ni in all the nickel sulfide NCs according to the following order: δ (β NiS) > δ (α NiS + β NiS) > δ (Ni_7S_6). The positive charge of Ni in nickel sulfide NCs is beneficial to the HER process[20]. The XPS results indicate that β NiS NCs have more positive charge, suggesting the best catalytic activity for HER.

3.2 Phase-dependent electrocatalytic properties of nickel sulfide NCs for HER

The HER electrocatalytic performance of the as-synthesized nickel sulfide NCs with different phases were evaluated in 0.5 M H_2SO_4 solution using a standard three-electrode system. Fig. 5A shows the LSV curves (*iR* corrected) of the bare GCE,

20% Pt/C, Ni_7S_6, α NiS + β NiS, and β NiS NCs with a scan rate of 5 $mV \cdot s^{-1}$. It can be seen that the bare GCE shows poor activity. Typically, the 20% Pt/C catalyst shows the highest electrocatalytic activity for HER with nearly zero overpotential. The onset overpotential for Ni_7S_6 NCs was about 208 mV, α NiS + β NiS and β NiS NCs exhibit similar onset overpotentials of about 186 mV. However, at the same potential, β NiS NCs show the highest HER current densities among nickel sulfide NCs. For example, when the potential was 250 mV, the HER current densities reached 2, 7 and 10 $mA \cdot cm^{-2}$ for Ni_7S_6, α NiS + β NiS, and β NiS NCs, respectively. Because the current density is proportional to the quantity of evolved hydrogen[21], and the larger current density reflects the better HER electrocatalytic behavior, therefore, it can be concluded that NiS NCs show superior HER catalytic activity than Ni_7S_6 NCs. In addition, β NiS NCs exhibit higher catalytic activity than α NiS NCs, further suggesting that the syngony of nickel sulfide NCs is also an important factor to affect the catalytic activities for HER.

The Tafel slope is another important factor to reflect the intrinsic property of the electrocatalyst materials, and the ideal electrocatalyst should has low Tafel slope. Fig. 5B shows the Tafel plots of the 20% Pt/C, Ni_7S_6, α NiS + β NiS, and β NiS NCs derived from the polarization curves fitted well with the Tafel equation ($\eta = a + b \log j$, where b is the Tafel slope and j is the current density). The Tafel slope for the 20% Pt/C, Ni_7S_6, α NiS + β NiS, and β NiS NCs is 30, 70.3, 58.5 and 51.2 $mV \cdot dec^{-1}$, respectively. These results indicate that β NiS NCs display the best electrocatalytic activity and the fastest HER rate of all the nickel sulfide NCs. Typically, the 20% Pt/C

catalyst shows the fastest HER rate. Furthermore, the Tafel slope also can be used to explain the reaction mechanism of HER. The values of all the nickel sulfide crystalline phases reveal that the HER occurs via a Volmer-Heyrovsky mechanism[22], that is to say, the first step is a fast discharge reaction (Equation (1)) and followed by a rate determining step, which is the electrochemical desorption of H_{ads} and H_3O^+ to produce hydrogen (Equation (2)).

Volmer reaction: $$H_3O^+ + e^- \rightarrow H_{ads} + H_2O \quad (1)$$

Heyrovsky reaction: $$H_3O^+ + e^- + H_{ads} \rightarrow H_2 + H_2O \quad (2)$$

To further insight into the electrocatalytic activity of nickel sulfide NCs with different phases, exchange current density (j_0) values of various catalysts have been calculated, as shown in Table 2. The values of j_0 were derived from Tafel plots by applying the extrapolation method (Fig. S1). The resulting j_0 of β NiS NCs is 2.4×10^{-6} $A\cdot cm^{-2}$, which is larger than 1.2×10^{-6} $A\cdot cm^{-2}$ of α NiS + β NiS and 1.74×10^{-7} $A\cdot cm^{-2}$ of Ni_7S_6 NCs. The j_0 values also confirmed that β NiS NCs exhibit the best electrocatalytic behavior for the HER. In order to further study the relationship between the catalytic activity toward HER and BET surface area for nickel sulfide NCs with different phases, the j_0 values were normalized by the BET surface areas (Table 2). It can be observed that the normalized j_0 values increased with the increase of BET surface areas, which indicates that the BET surface area is another factor to influence the electrocatalytic performance. In addition, we also found that the increased normalized j_0 values are not linear. For example, the BET surface area of β NiS is 5.6 times than that of Ni_7S_6 NCs, but the normalized j_0 value of β NiS is 8

times than that of the Ni_7S_6 NCs. These observations indicate that BET surface area of a catalyst is not a dominant factor in determining catalytic activity for HER[23]. Then we further estimate the effective electrochemical active surface area (ECSA) of the as-synthesized nickel sulfide NCs according to the reported method by measuring the electrochemical double-layer capacitances (C_{dl}) because C_{dl} are believed to be positively proportional to ECSA[24]**.** The values of C_{dl} were measured by CV curves (Fig. 6A-C) at non-Faradaic potentials (0.1-0.2 V), which could be mostly considered as the double-layer capacitive behavior. The C_{dl} was estimated by plotting the $\Delta j = j_a - j_c$ at the middle potential (0.15 V) against the CV scan rates (Fig. 6D), where the slope is twice C_{dl}. As shown in Table 2, β NiS NCs exhibit much larger C_{dl} (2.7 $mF \cdot cm^{-2}$) than that of the Ni_7S_6 NCs (1.0 $mF \cdot cm^{-2}$) and α NiS + β NiS NCs (1.6 $mF \cdot cm^{-2}$), suggesting the high exposure of effective electrochemical active sites of β NiS NCs, which can be used to explain the excellent HER activity[25].

Besides the catalytic activity, the excellent stability of electrocatalyst is also an important requirement. A long-term potential sweeps of Ni_7S_6, α NiS + β NiS, and β NiS NCs were performed (Fig. 7A). It is observed that β NiS NCs exhibit good stability in acidic solution with slight current loss after 1000 cycles. However, the current loss of α NiS + β NiS NCs was larger. The Ni_7S_6 NCs show the largest current loss among all the samples after 1000 cycles. Furthermore, the time-dependent current density curve of (Fig. 7B) the as-synthesized nickel sulfide NCs under static overpotential of 200 mV have been provided to offer more information about the long-term electrochemical stability. The results indicate that the current densities of

all the as-synthesized nickel sulfide NCs have a slight degradation after a long period of 50 000 s. The formation of typical serrate shape in the as-measured time-dependent curve can be attributed to the accumulation and release of hydrogen bubbles[26].

In order to understand the kinetics process of the as-synthesized catalysts under HER, the EIS experiments were performed in 0.5 M H_2SO_4 with frequencies ranging from 100 kHz to 0.1 Hz at different overpotentials from 100 to 200 mV. The Nyquist plots of the Ni_7S_6, α NiS + β NiS and β NiS NCs are shown in Fig. 8A-C. It can be observed that all the semicircles diameter of the as-synthesized nickel sulfide NCs decreased gradually with the increase of potential from 100 to 200 mV, which indicates that all the as-synthesized nickel sulfide NCs have good electron transfer ability at high potential. In addition, the corresponding Bode plots (Fig. 8D-F) suggest a one-time constant process for all the nickel sulfide NCs, and thus we use a simple equivalent electrical circuit to describe the HER process, as shown in Fig. S2, the corresponding fitting results are listed in Table S1. As we all know, the value of charge transfer resistance (R_{ct}) has a relationship with the electrocatalysis kinetics, the lower of R_{ct}, the faster of reaction rate[27]. It can be seen from Table S1 that the R_{ct} values of all the catalysts are potential-dependent. Furthermore, we also found that the β NiS NCs exhibit the smallest R_{ct} among all the catalysts at the same overpotential, indicating the highest electrical conductivity of β NiS NCs, which is also responsible for the remarkable HER activity.

According to the above results, the excellent catalytic activity and stability of β NiS NCs can be attributed to the following reasons. First, from the electronic effect, the β

NiS NCs have more positive charge of Ni (as proved by XPS), which can enhance the HER process. Second, the β NiS NCs have more BET surface area (as proved by N_2 sorption) and effective electrochemical active sites (as reflected from the C_{dl} values), which is beneficial to the HER. Finally, the β NiS NCs exhibit the smallest charge transfer resistance (as proved by EIS), which is beneficial to the electronic transport, thus, the HER efficiency was improved. In short, due to the different crystalline phase structure, the as-synthesized nickel sulfide NCs exhibit different catalytic activity for HER.

4 Conclusion

Nanostructured nickel sulfide with different phases have been successfully synthesized via a thermal decomposition approach using nickel acetylacetonate as the nickel source, 1-dodecanethiol as the sulfur source and oleylamine as the solvent. Phase evolution of nickel sulfide NCs can be easily achieved by changing the molar ratio of Ni:S precursor and the species of solvent. Generally, a higher Ni:S precursor ratio (Ni:S = 0.36) is beneficial for forming the Ni_7S_6 phase. Decreasing the Ni:S precursor ratio results in the phase evolution from Ni_7S_6 to β NiS phase. By changing the reaction solvent, the β NiS NCs were transformed to the mixture syngony of α NiS and β NiS phases. Electrochemical measurements indicate that the as-synthesized β NiS NCs exhibit much better catalytic activity than the Ni_7S_6 and α NiS + β NiS NCs for HER. Because of the different crystalline phase structure of the as-synthesized nickel sulfide NCs, the β NiS NCs show excellent electrocatalytic activity with a low onset overpotential (186 mV), a small Tafel slope (51.2 $mV \cdot dec^{-1}$), a high exchange

current density (2.4×10^{-6} A·cm^{-2}), a large electrochemical double-layer capacitances (2.7 mF·cm^{-2}) and good stability. In addition, the high electrical conductivity of β NiS NCs also enhanced the catalytic activity for HER. This study demonstrates that the nanostructure and appropriate atomic configuration of nickel sulfide catalysts is important for affecting the electrocatalytic performance in HER.

Acknowledgements

This work was supported by the National Natural Science Foundation of China (Grants No. 21006128, 21176258, U1162203), the Fundamental Research Funds for the Central Universities (Grants No. 15CX06039A) and the Specialized Research Fund for the Doctoral Program of Higher Education of China (Grant No. 20110133110002).

References

1 (a) W. Hu, *Int. J. Hydrogen Energy*, 2000, **25**, 111. (b) J. Tian, Q. Liu, A. M. Asiri, X. Sun, *J. Am. Chem. Soc.*, 2014, **136**, 7587.

2 K. Xiong, L. Li, Z. Deng, M. Xia, S. Chen, S. Tan, X. Peng, C. Duan, Z. Wei, *RSC Adv.*, 2014, **4**, 20521.

3 T. F. Jaramillo, K. P. Jørgensen, J. Bonde, J. H. Nielsen, S. Horch, I. Chorkendorff, *Science*, 2007, **317**, 100.

4 (a) Y. Pan, Y. Liu, C. Liu, *J. Power Sources*, 2015, **285**, 169. (b) Y. Pan, W. Hu, D. Liu, Y. Liu, C. Liu, *J. Mater. Chem. A*, 2015, **3**, 13087.

5 L. Liao, S. Wang, J. Xiao, X. Bian, Y. Zhang, M. D. Scanlon, X. Hu, Y. Tang, B. Liu, H. H. Girault, *Energy. Environ. Sci.*, 2014, **7**, 387.

6 (a) D. Merki, X. Hu, *Energy Environ. Sci.*, 2011, **4**, 3878. (b) Y. Li, H. Wang, L. Xie, Y. Liang, G. Hong, H. Dai, *J. Am. Chem. Soc.*, 2011, **133**, 7296.

7 (a) Q. Han, K. Liu, J. Chen, X. Wei, *Int. J. Hydrogen Energy*, 2003, 28, 12072. (b) I. Paseka, *Electrochim. Acta*, 1993, **38**, 2449.

8 H. Y. Su, Y. Gorlin, I. C. Man, F. Calle-Vallejo, J. K. Norskov, T. F. Jaramillo, J. Rossmeisl, *Phys. Chem. Chem. Phys.*, 2012, **14**, 14010.

9 Y. Wang, J. Wu, Y. Tang, X. Lü, C. Yang, M. Qin, F. Huang, X. Li, X. Zhang, *ACS Appl. Mater. Interfaces*, 2012, **4**, 4246.

10 J. F. Callejas, C. G. Read, E. J. Popczun, J. M. McEnaney, R. E. Schaak, *Chem. Mater.*, 2015, **27**, 3769.

11 Y. Pan, Y. Liu, J. Zhao, K. Yang, J. Liang, D. Liu, W. Hu, D. Liu, Y. Liu, C. Liu, *J. Mater. Chem. A*, 2015, **3**, 1656.

12 J. Park, B. Koo, K. Y. Yoon, Y. Hwang, M. Kang, J. G. Park, T. Hyeon, *J. Am. Chem. Soc.*, 2005, **127**, 8433.

13 Q. Yuan, A. X. Yin, C. Luo, L. D. Sun, Y. W. Zhang, W. T. Duan, H. C. Liu, and C. H. Yan, *J. Am. Chem. Soc.*, 2008, **130**, 3465.

14 B. You, N. Jiang, M. Sheng, Y. Sun, *Chem. Commun.*, 2015, **51**, 4252.

15 L. Cao, D. Chen, W. Li, and R. A. Caruso, *ACS Appl. Mater. Interfaces*, 2014, **6**, 13129.

16 C. Chen, Y. Yu, W. Li, C. Cao, P. Li, Z. Dou and W. Song, *J. Mater. Chem.*, 2011, **21**, 12836.

17 Q. Liu, J. Zhang, *CrystEngComm*, 2013, **15**, 5087.

18 X. Wu, B. Yang, Z. Li, L. Lei, X. Zhang, *RSC Adv.*, 2015, **5**, 32976.

19 L. Yin, Y. P. Yuan, S. W. Cao, Z. Zhang, C. Xue, *RSC Adv.*, 2014, **4**, 6127.

20 D. Y. Chung, J. W. Han, D. H. Lim, J. H. Jo, S. J. Yoo, H. Lee, Y. E. Sung, *Nanoscale*, 2015, **7**, 5157.

21 J. F. Xie, H. Zhang, S. Li, R. X. Wang, X. Sun, M. Zhou, X. W. Lou, Y. Xie, *Adv. Mater.*, 2013, **25**, 5807.

22 (a) Y. F. Xu, M. R. Gao, Y. R. Zheng, J. J. Jiang, S. H. Yu, *Angew. Chem. Int. Ed.*, 2013, **52**, 8546. (b) C. G. Morales-Guio, L. A. Stern, X. L. Hu, *Chem. Soc. Rev.*, 2014, **43**, 6555.

23 Z. Z. Wu, B. Z. Fang, A. Bonakdarpour, A. K. Sun, D. P. Wilkinson, D. Z. Wang, *Appl. Catal. B-Environ.*, 2012, **125**, 59.

24 M. A. Lukowski, A. S. Daniel, F. Meng, A. Forticaux, L. Li, S. Jin, *J. Am. Chem. Soc.*, 2013, **135**, 10274.

25 J. F. Xie, J. J. Zhang, S. Li, F. Grote, X. D. Zhang, H. Zhang, R. X. Wang, Y. Lei, B. C. Pan, Y. Xie, *J. Am. Chem. Soc.*, 2013, **135**, 17881.

26 S. Gu,H. Du, A. M. Asiri, X. Sun and C. M. Li, *Phys. Chem. Chem.Phys.*, 2014, **16**, 16909.

27 L. Liao , J. Zhu , X. J. Bian , L. Zhu , M. D. Scanlon , H. H. Girault , B. Liu, *Adv. Funct. Mater.*, 2013, **23**, 5326.

Figure Captions

Fig. 1 XRD patterns of the as-synthesized nickel sulfide NCs at different synthetic conditions of (A) Ni:S = 0.36 in OAm, (B) Ni:S = 0.08 in OAm, (C) Ni:S = 0.18 in ODE, (D) Ni:S = 0.18 in OAm, respectively.

Fig. 2 TEM images of the as-synthesized nickel sulfide NCs at different synthetic conditions of (A) Ni:S = 0.36, (B) Ni:S = 0.18, (D) Ni:S = 0.08, (F) Ni:S = 0.18 in ODE, respectively. HRTEM images of (C) Ni_7S_6 and (E) β NiS NCs. SEM images (G and H), elemental mapping of Ni (I) and S (J) elements and EDS (G) of the as-synthesized β NiS NCs.

Fig. 3 Nitrogen sorption isotherms (A) and pore-size distribution curves (B) for Ni_7S_6, α NiS + β NiS and β NiS NCs.

Fig. 4 XPS spectra in the Ni 2p and S 2p regions of the as-synthesized β NiS (A and B), α NiS + β NiS (C and D) and Ni_7S_6 NCs (E and F), respectively.

Fig. 5 (A) LSV curves (*iR* corrected) of the bare GCE, 20% Pt/C, Ni_7S_6, α NiS + β NiS, and β NiS NCs with a scan rate of 5 $mV \cdot s^{-1}$ in 0.5 M H_2SO_4 solution. (B) Tafel plots of the 20% Pt/C, Ni_7S_6, α NiS + β NiS, and β NiS NCs derived from the polarization curves.

Fig. 6 (A-C) Cyclic voltammetry curves of the as-synthesized Ni_7S_6, α NiS + β NiS and β NiS NCs in 0.5 M H_2SO_4 solution in the region of 0.1-0.2 V vs. RHE with different scan rates from 20 $mV \cdot s^{-1}$ to 180 $mV \cdot s^{-1}$. (D) The differences in current density variation ($\Delta J = J_a - J_c$) at an overpotential of 0.15 V plotted against scan rate fitted to a linear regression enables the estimation of C_{dl}.

Fig. 7 (A) Stability test for the Ni_7S_6, α NiS + β NiS and β NiS NCs with initial LSV

polarization curve and after 1000 cycles. (B) Time-dependent current density curve of the as-synthesized nickel sulfide NCs under static overpotential of 200 mV.

Fig. 8 (A-C) Nyquist plots of the Ni_7S_6, α NiS + β NiS and β NiS NCs in 0.5 M H_2SO_4 with frequencies ranging from 100 kHz to 0.1 Hz at different overpotentials from 100 to 200 mV. (D-F) the corresponding Bode plots of the Ni_7S_6, α NiS + β NiS and β NiS NCs, respectively.

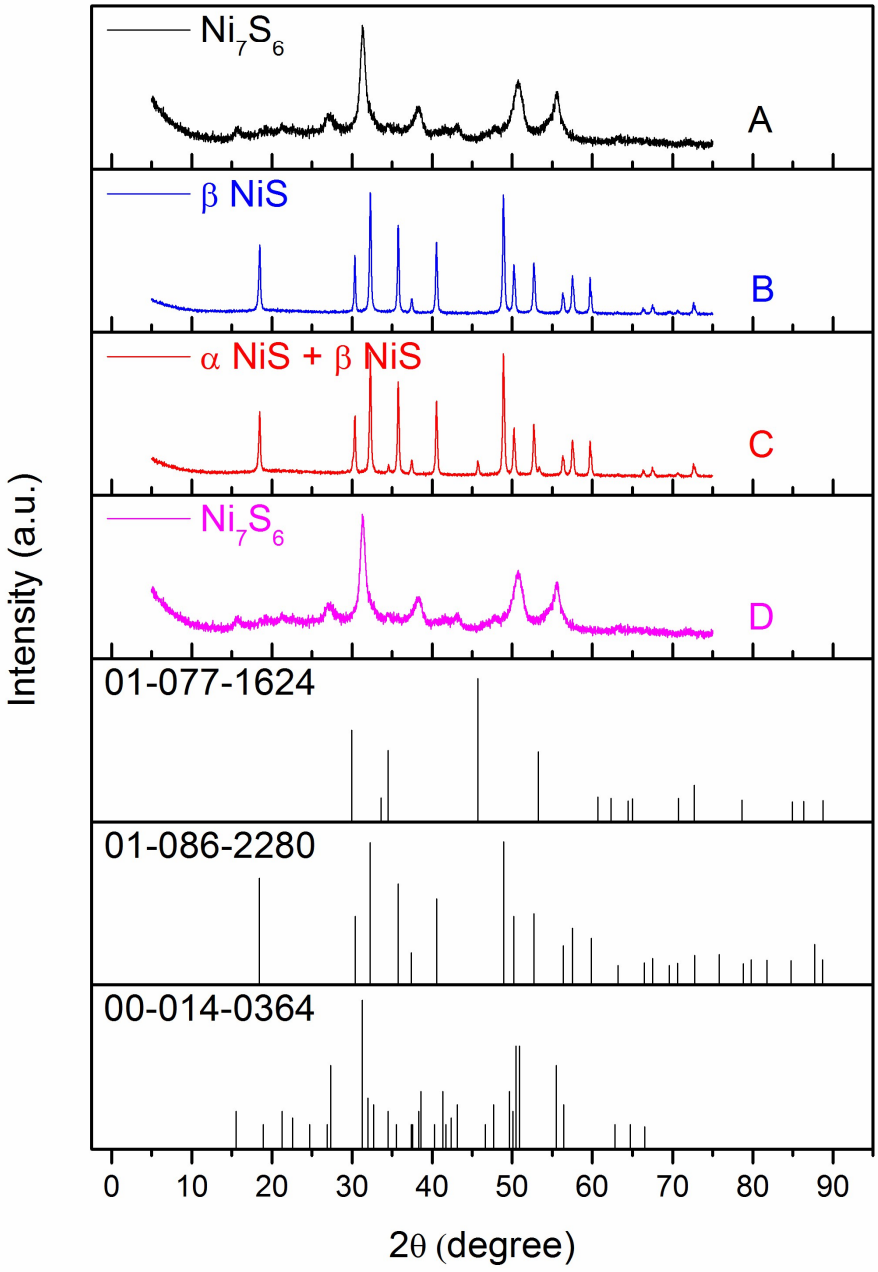

Fig. 1 XRD patterns of the as-synthesized nickel sulfide NCs at different synthetic conditions of (A) Ni:S = 0.36 in OAm, (B) Ni:S = 0.08 in OAm, (C) Ni:S = 0.18 in ODE, (D) Ni:S = 0.18 in OAm, respectively.

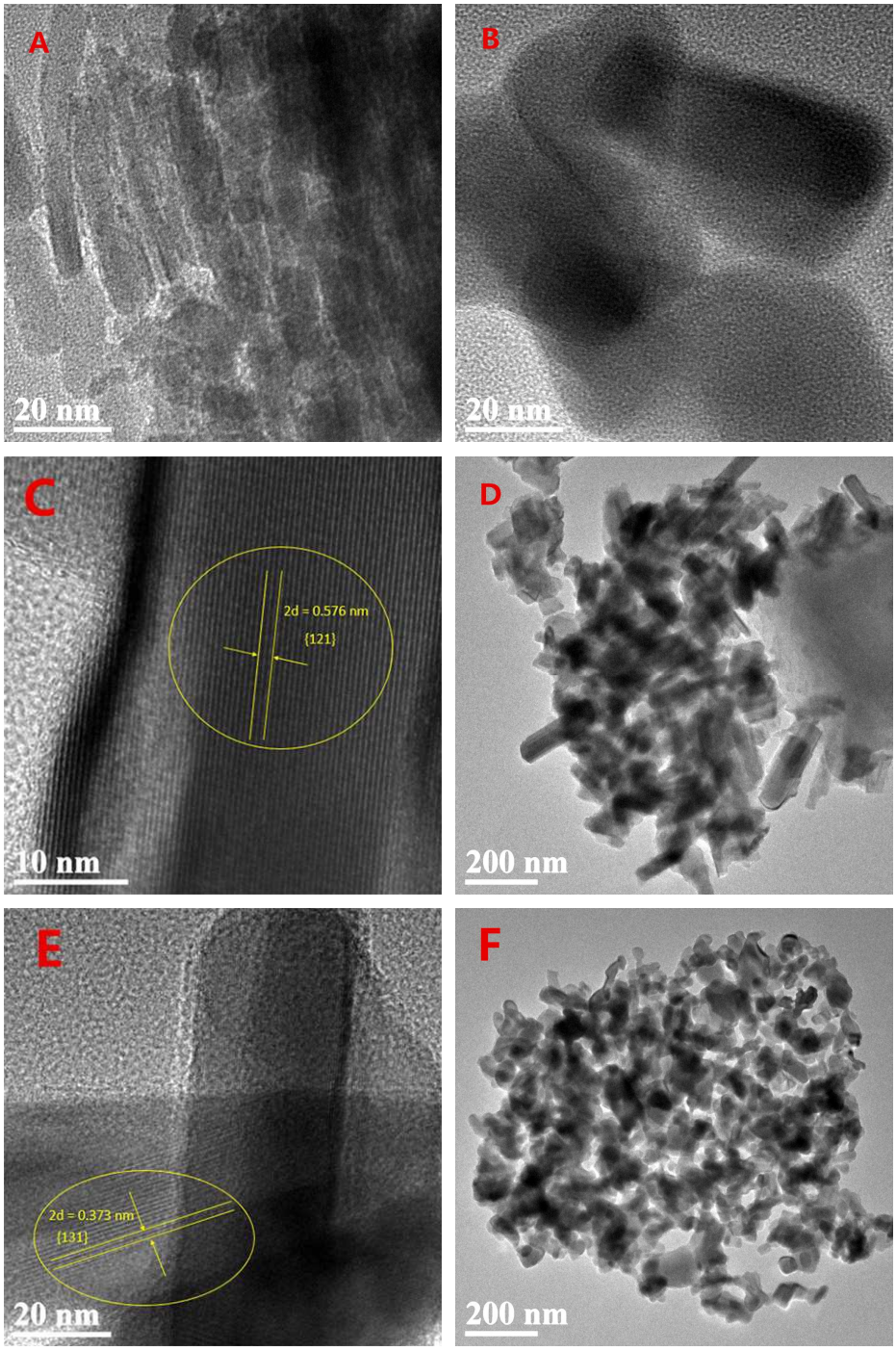

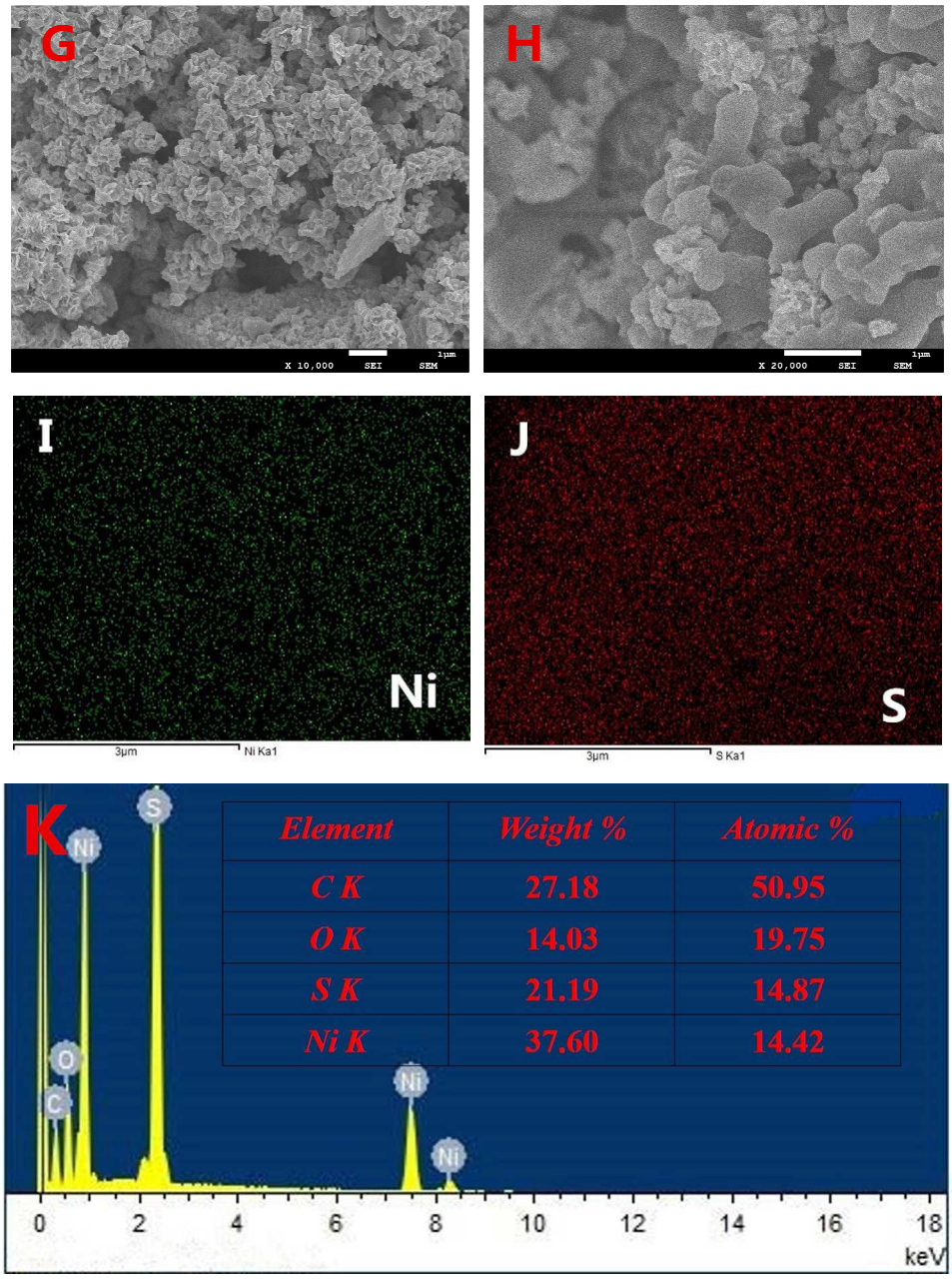

Fig. 2 TEM images of the as-synthesized nickel sulfide NCs at different synthetic conditions of (A) Ni:S = 0.36, (B) Ni:S = 0.18, (D) Ni:S = 0.08, (F) Ni:S = 0.18 in ODE, respectively. HRTEM images of (C) Ni_7S_6 and (E) β NiS NCs. SEM images (G and H), elemental mapping of Ni (I) and S (J) elements and EDS (G) of the as-synthesized β NiS NCs.

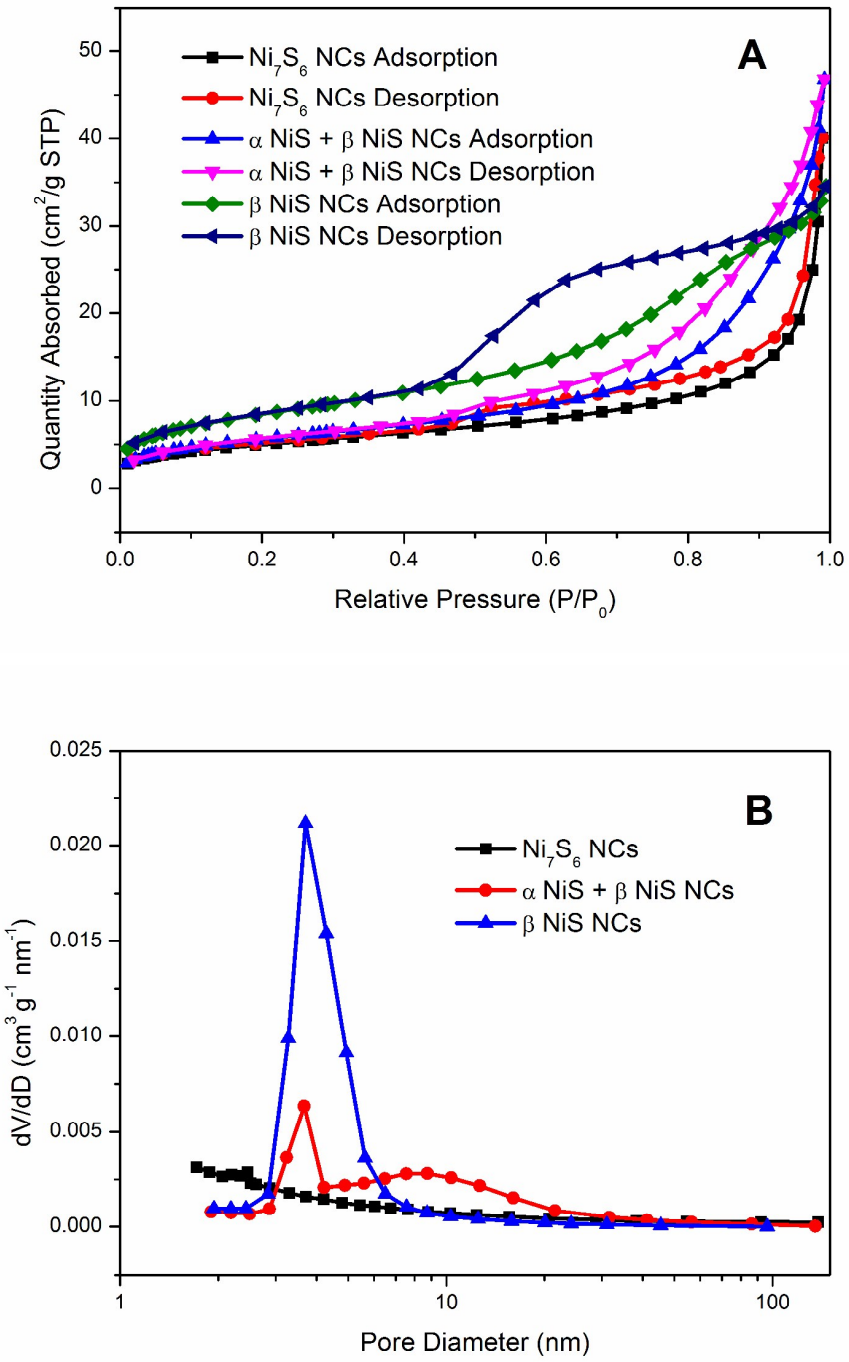

Fig. 3 Nitrogen sorption isotherms (A) and pore-size distribution curves (B) for Ni_7S_6, α NiS + β NiS and β NiS NCs.

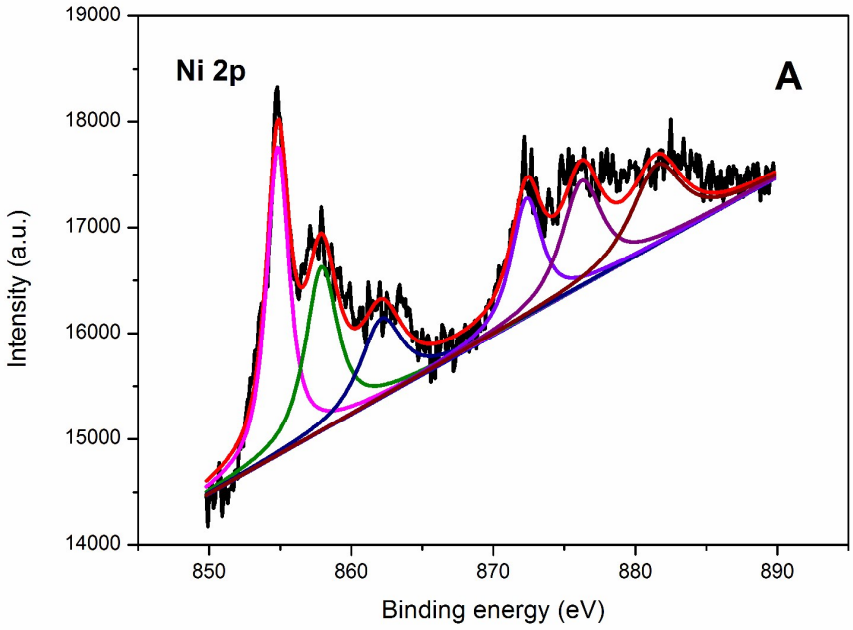

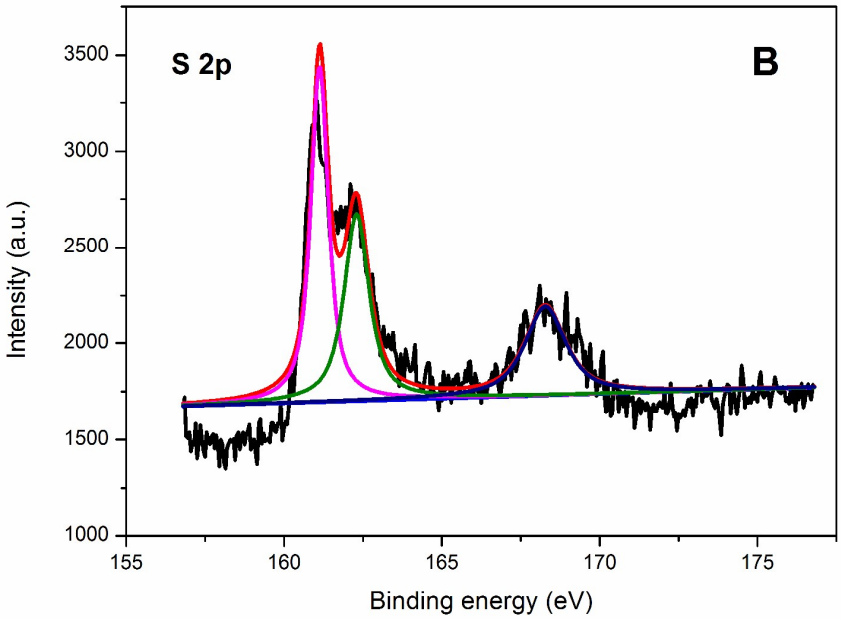

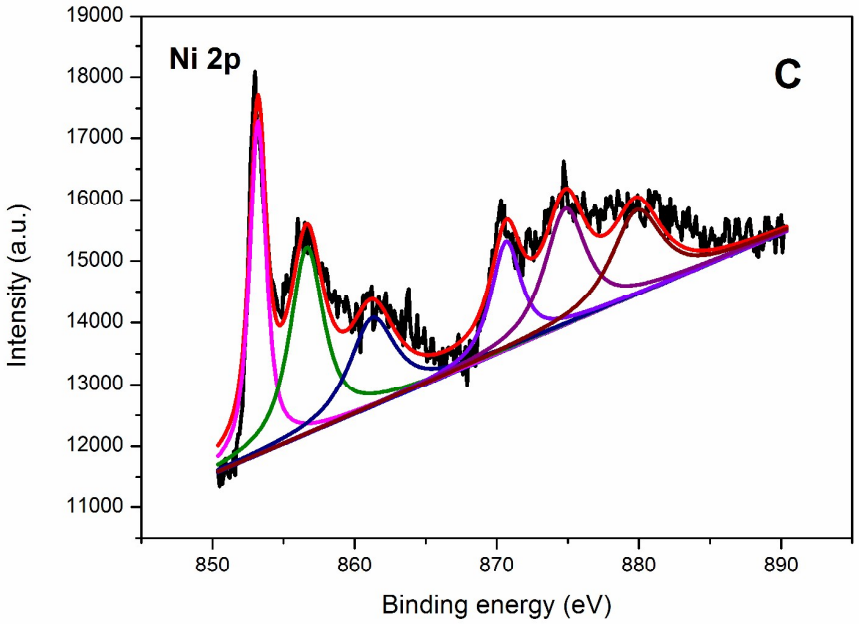

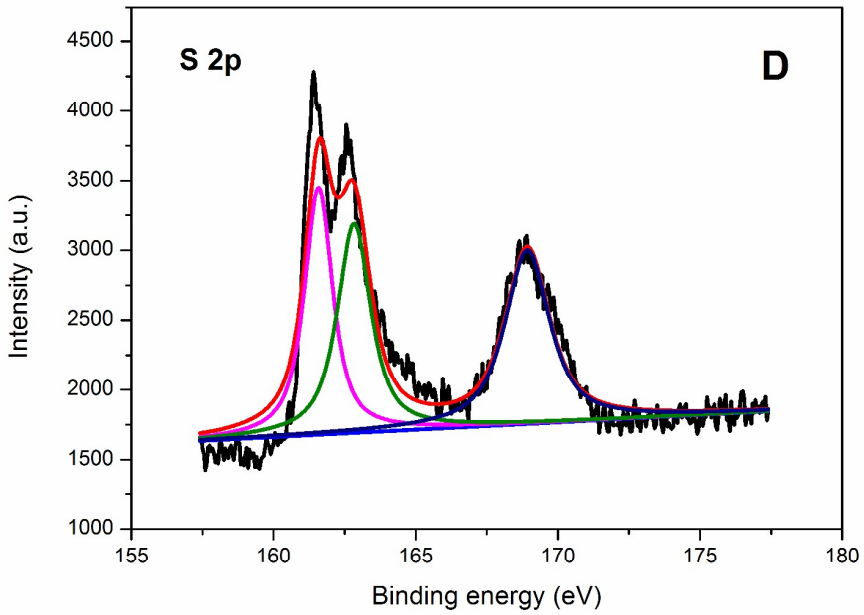

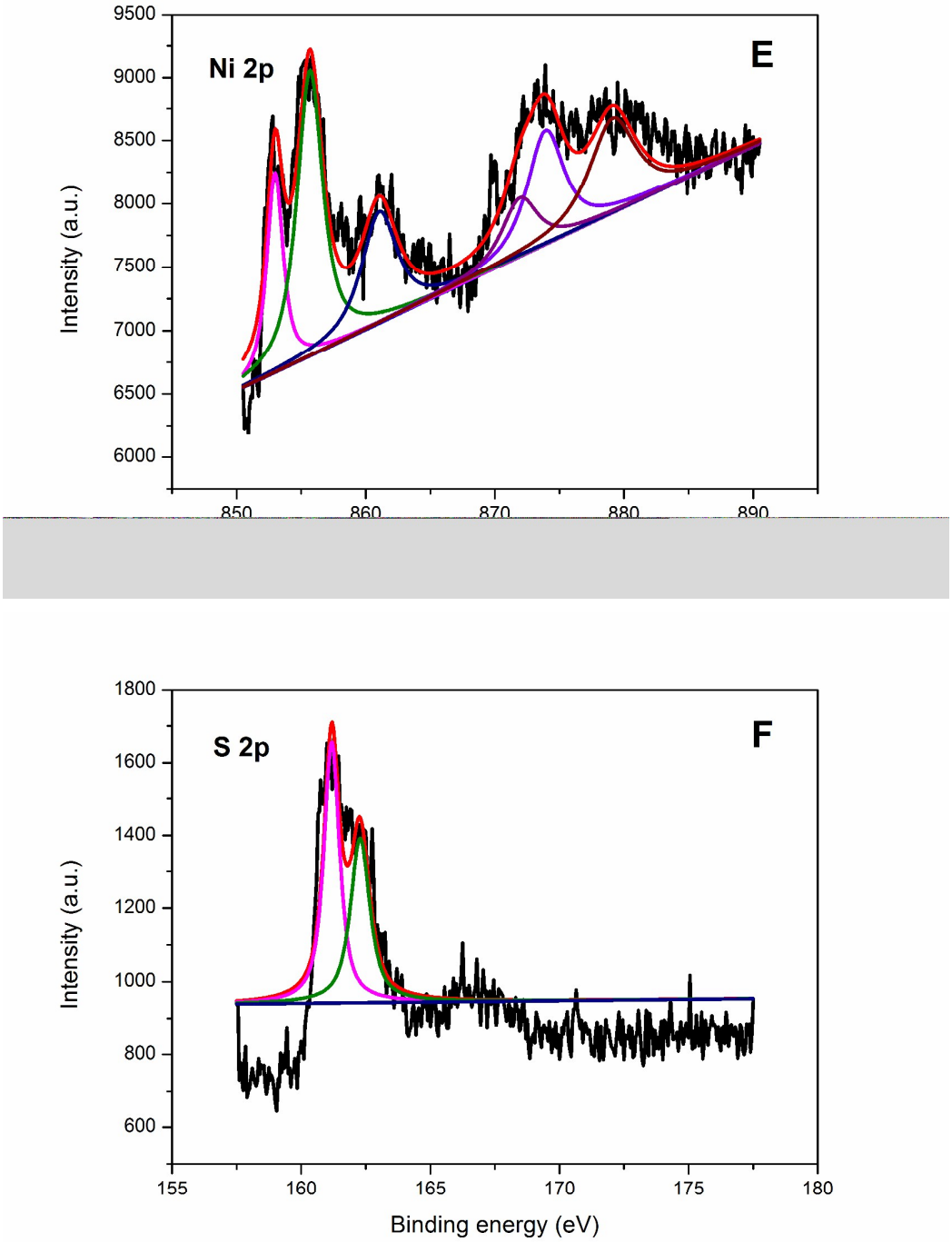

Fig. 4 XPS spectra in the Ni 2p and S 2p regions of the as-synthesized β NiS (A and B), α NiS + β NiS (C and D) and Ni_7S_6 NCs (E and F), respectively.

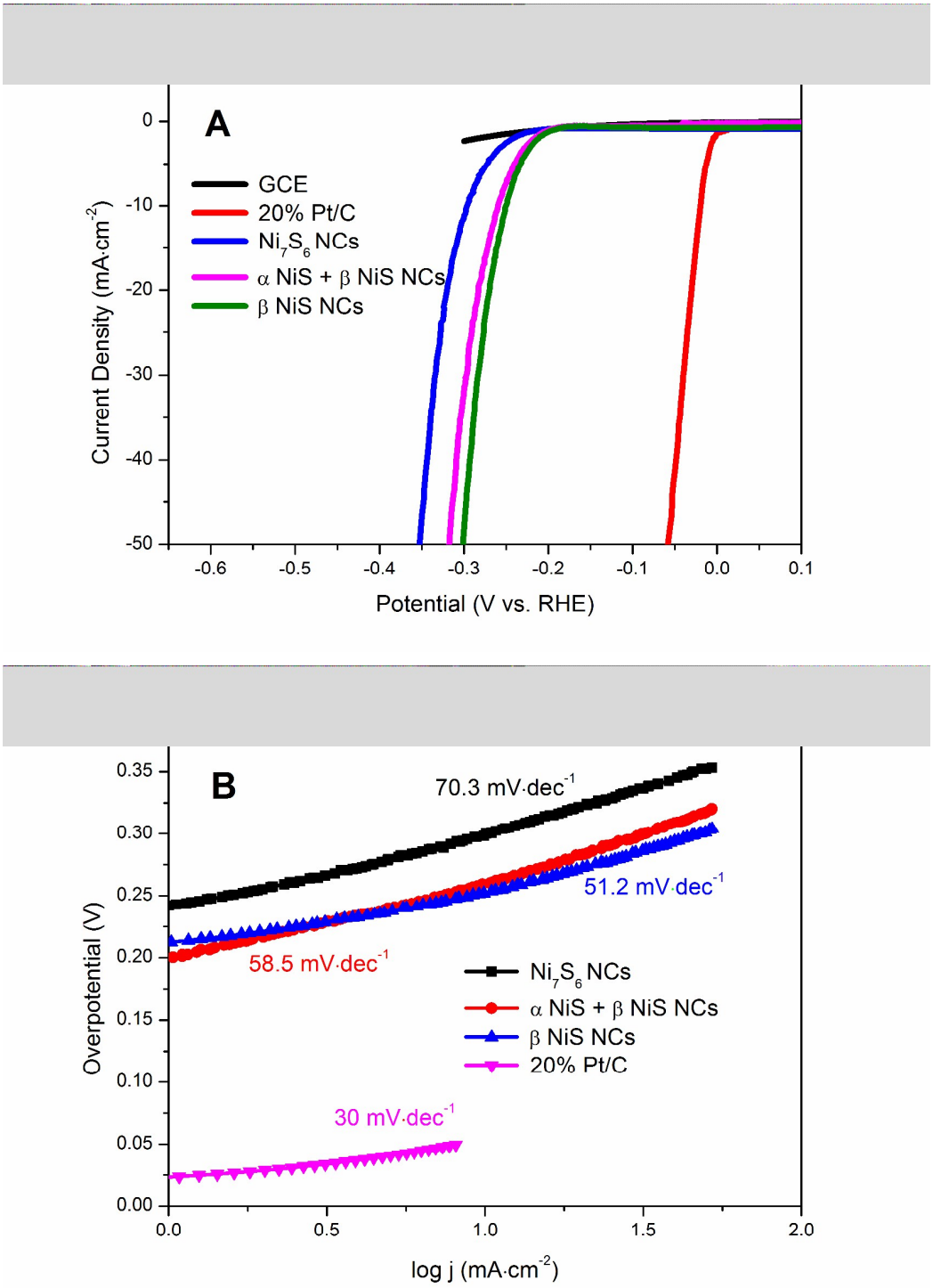

Fig. 5 (A) LSV curves (*iR* corrected) of the bare GCE, 20% Pt/C, Ni_7S_6, α NiS + β NiS, and β NiS NCs with a scan rate of 5 $mV \cdot s^{-1}$ in 0.5 M H_2SO_4 solution. (B) Tafel plots of the 20% Pt/C, Ni_7S_6, α NiS + β NiS, and β NiS NCs derived from the

polarization curves.

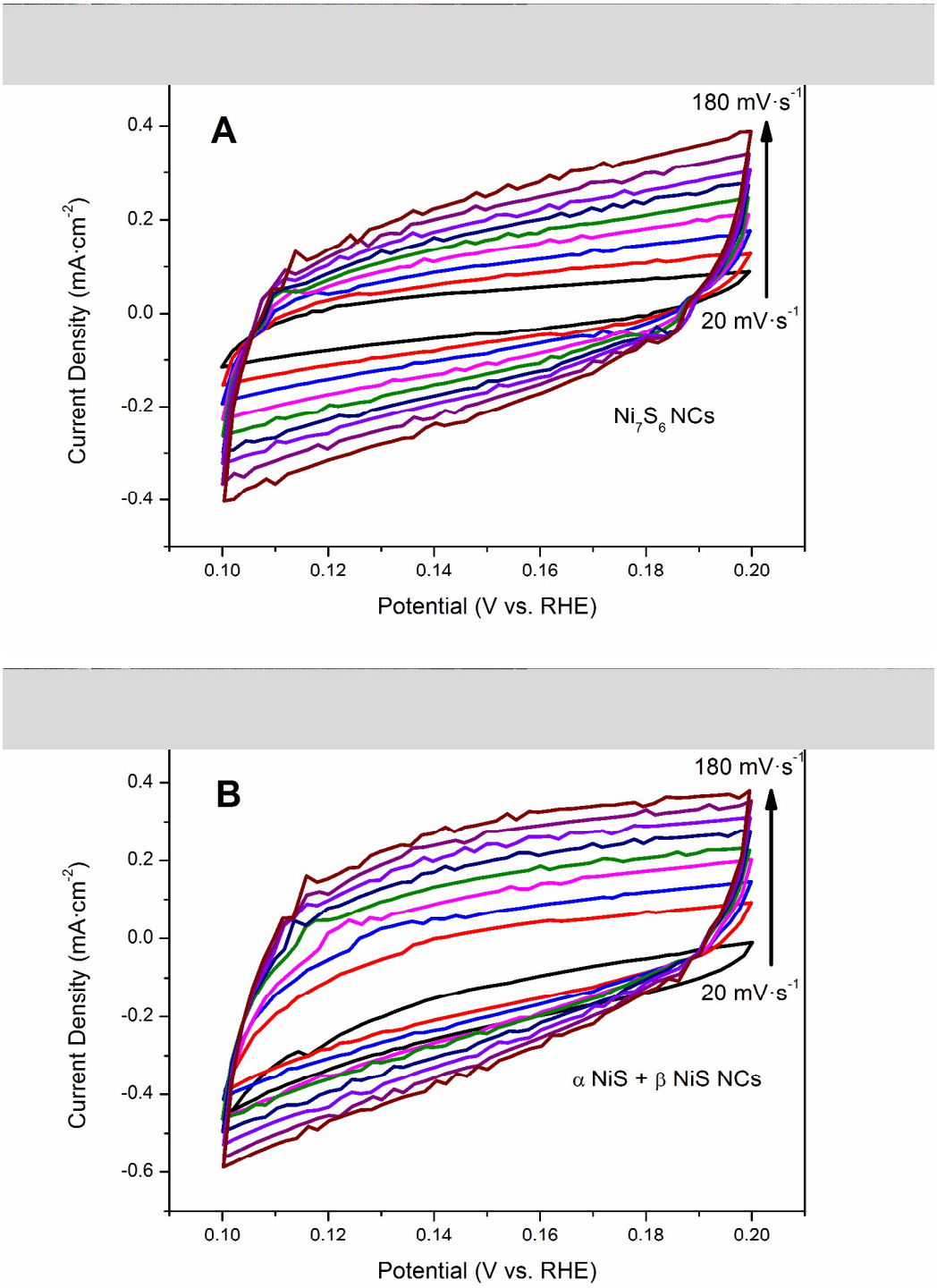

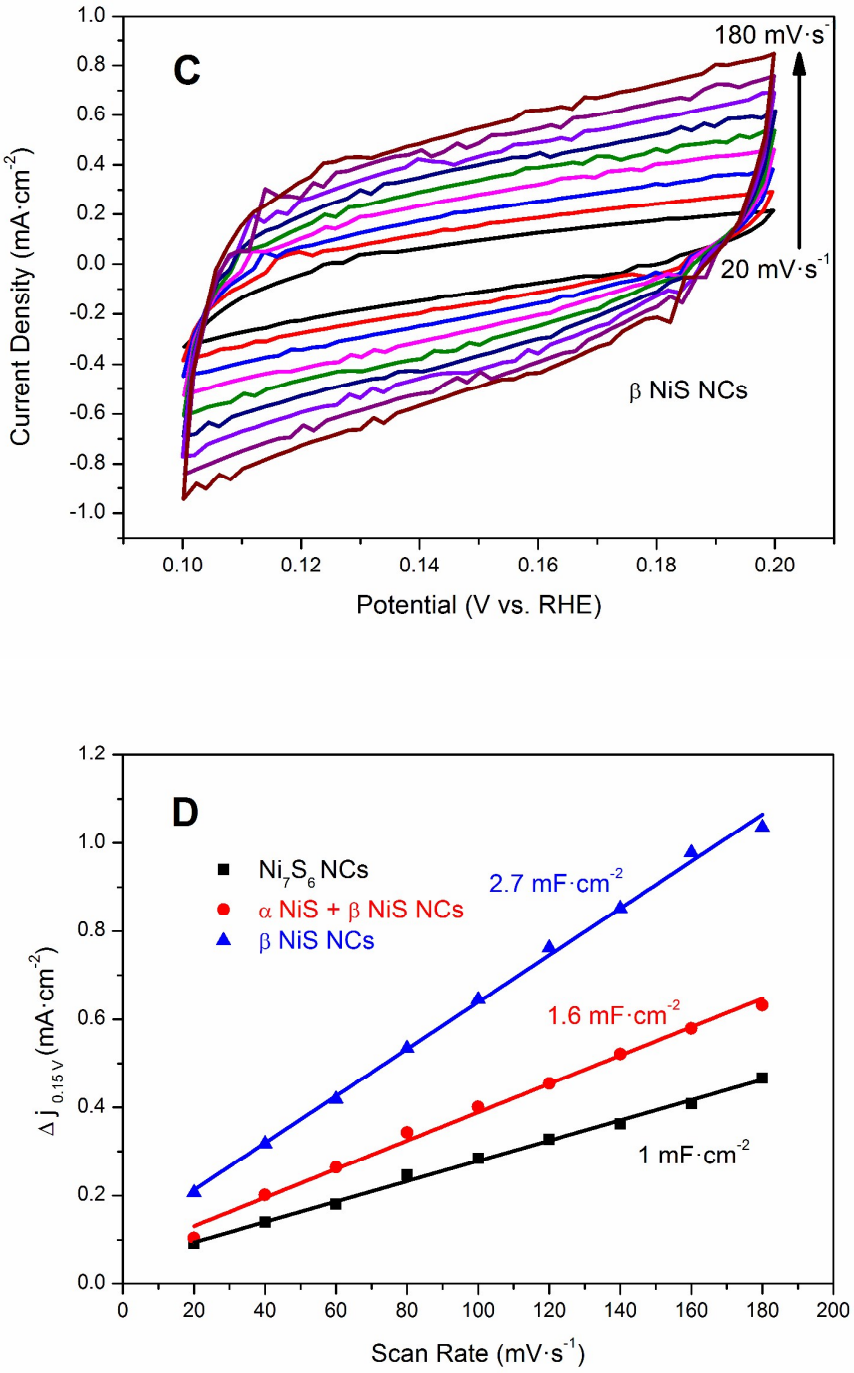

Fig. 6 (A-C) Cyclic voltammetry curves of the as-synthesized Ni_7S_6, α NiS + β NiS and β NiS NCs in 0.5 M H_2SO_4 solution in the region of 0.1-0.2 V vs. RHE with different scan rates from 20 $mV \cdot s^{-1}$ to 180 $mV \cdot s^{-1}$. (D) The differences in current

density variation ($\Delta J=J_a-J_c$) at an overpotential of 0.15 V plotted against scan rate fitted to a linear regression enables the estimation of C_{dl}.

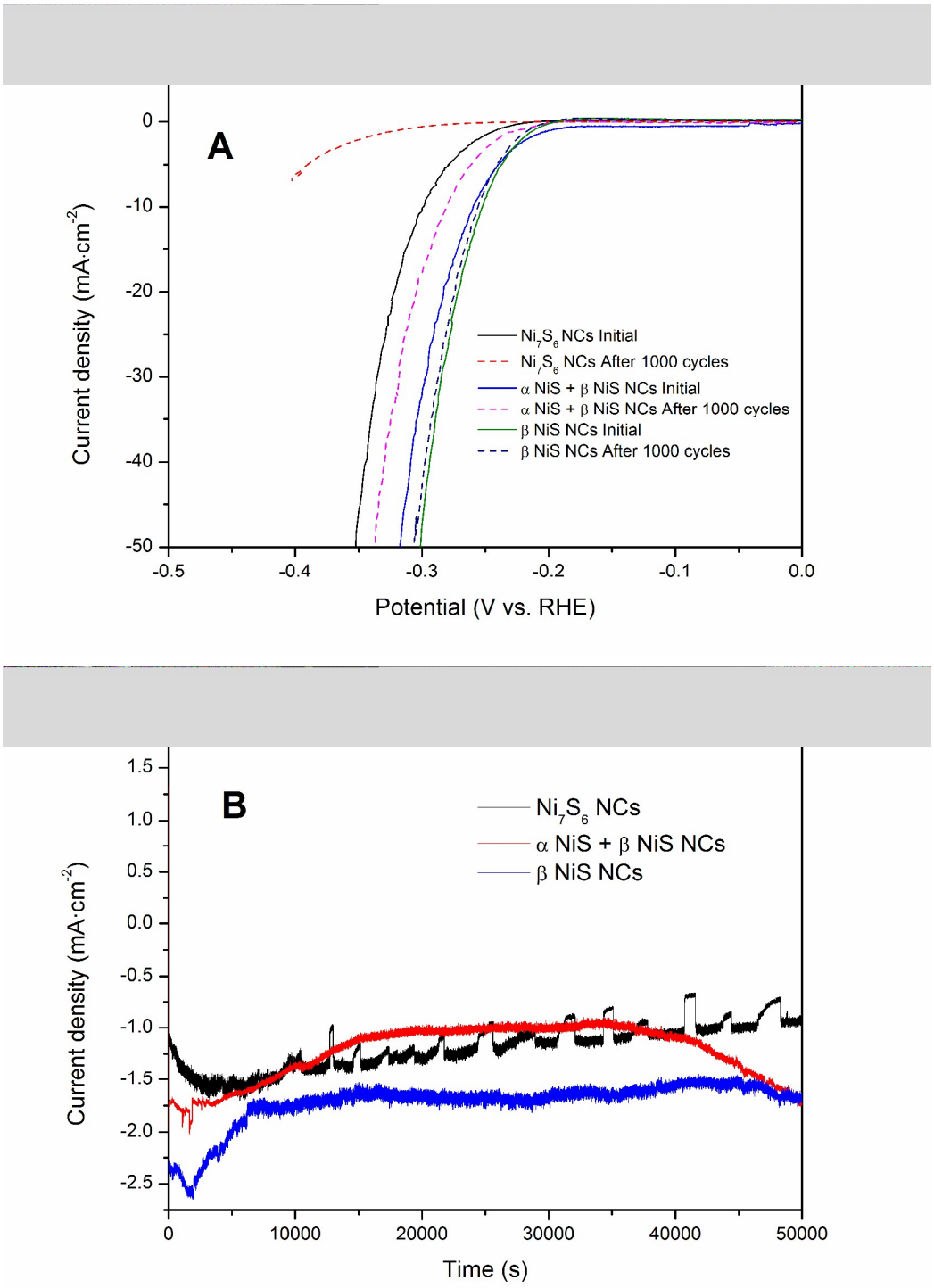

Fig. 7 (A) Stability test for the Ni_7S_6, α NiS + β NiS and β NiS NCs with initial LSV

polarization curve and after 1000 cycles. (B) Time-dependent current density curve of the as-synthesized nickel sulfide NCs under static overpotential of 200 mV.

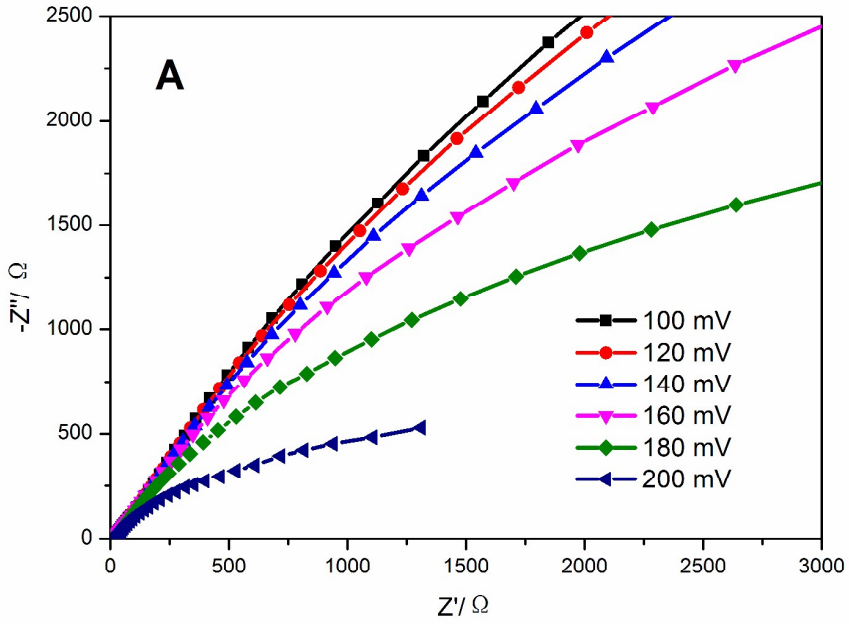

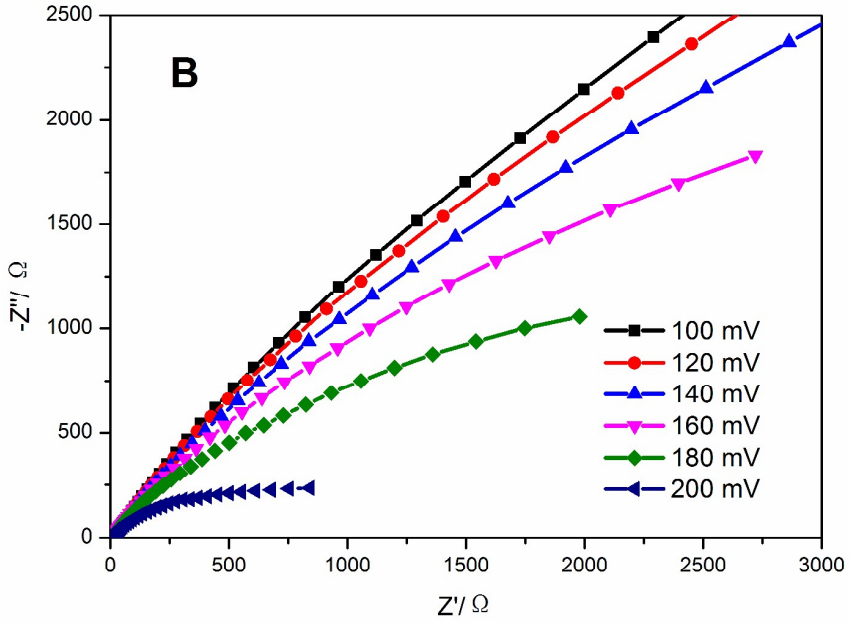

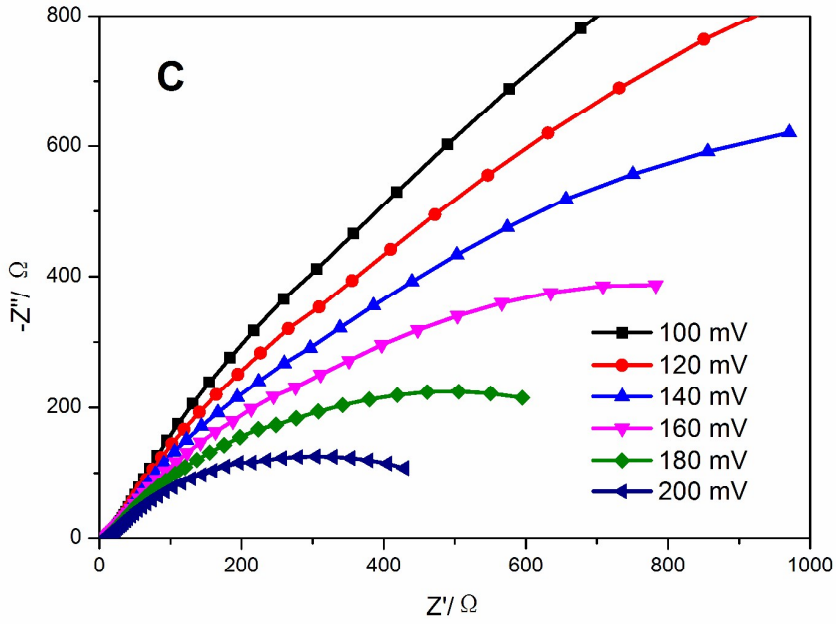

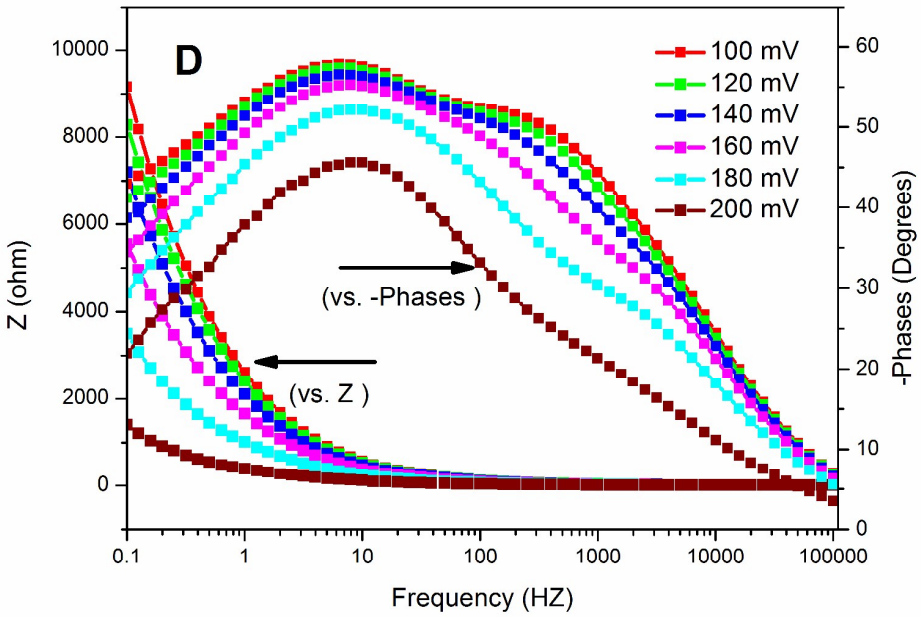

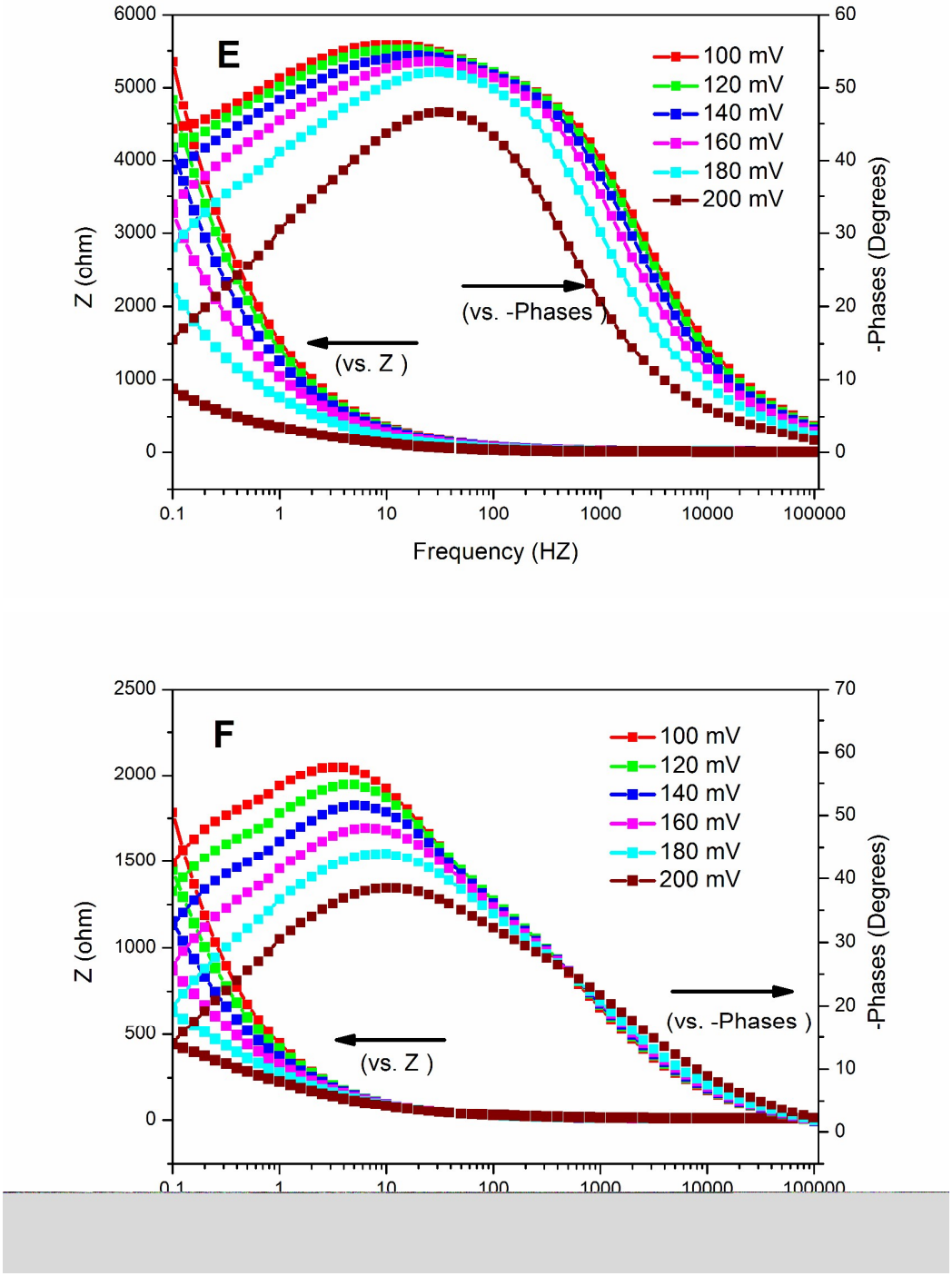

Fig. 8 (A-C) Nyquist plots of the Ni_7S_6, α NiS + β NiS and β NiS NCs in 0.5 M H_2SO_4 with frequencies ranging from 100 kHz to 0.1 Hz at different overpotentials from 100 to 200 mV. (D-F) the corresponding Bode plots of the Ni_7S_6, α NiS + β NiS

and β NiS NCs, respectively.

Table 1 Detailed synthetic conditions of the single-factor experiment.

Group	T (^{o}C)	t (h)	Ni:S	Solvent	Product
A	280	5	0.36	OAm	Ni_7S_6
B	280	5	0.08	OAm	β NiS
C	280	5	0.18	ODE	α NiS + β NiS
D	280	5	0.18	OAm	Ni_7S_6

Table 2 BET surface areas and catalytic activities toward HER for Ni_7S_6, α NiS + β NiS and β NiS NCs.

Catalyst	S_{BET} ($m^2 \cdot g^{-1}$)	log j ($mA \cdot cm^{-2}$)	j_0 ($A \cdot cm^{-2}$)	Normalized j_0 ($A \cdot cm^{-2}_{BET}$)	C_{dl} ($mF \cdot cm^{-2}$)
Ni_7S_6	17.6	-3.76	1.74×10^{-7}	4.97×10^{-9}	1.0
α NiS + β NiS	20.3	-2.92	1.2×10^{-6}	2.97×10^{-8}	1.6
β NiS	30.4	-2.62	2.4×10^{-6}	3.96×10^{-8}	2.7

Graphic Abstract

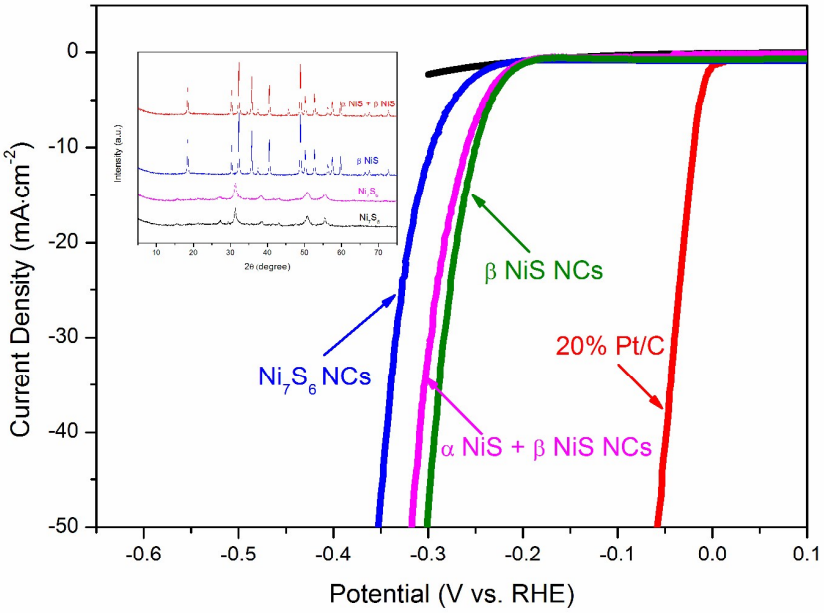

Nanostructured nickel sulfide with different phases were synthesized and the electrocatalytic activity for the hydrogen evolution reaction were investigated. β NiS exhibits the best catalytic activity among all the nickel sulfide catalysts. This study provides a good strategy for designing more efficient nickel sulfide catalysts.